Received: 19 April 2021 | Revised: 17 June 2021 | Accepted: 9 July 2021

IET Power Electronics

DOI: 10.1049/pel2.12174

The Institution of Engineering and Technology WILEY

ORIGINAL RESEARCH PAPER

Maximizing power utilization of dual converter using predictive control with steady state cost

Martin Votava | **Vaclav Smidl** | **Zdenek Peroutka** | **Tomas Glasberger**

Research and Innovation Centre for Electrical Engineering, University of West Bohemia, Pilsen, Czech Republic

Correspondence
Martin Votava, Research and Innovation Centre for Electrical Engineering, University of West Bohemia, Pilsen, Univerzitni 26, Plzen 301 00, Czech Republic.
Email: mvotava@fel.zcu.cz

Funding information
Ministry of Education, Youth and Sports of the Czech Republic under the project OP VVV Electrical Engineering Technologies with High-Level of Embedded Intelligence, Grant/Award Number: CZ.02.1.01/0.0/0.0/18_069/0009855

Abstract

Capability to deliver maximum power of a converter is essential for increasing power density that is limiting in many applications. Therefore, control algorithm should guarantee operation within converter thermal limits. This requirement can be formalized by a hard constraint in the cost function of model predictive control (MPC). However, the temperatures of the converter elements are not constant in the steady state, which complicates evaluation of the cost on long prediction horizon. Therefore, the evaluation is simplified utilizing the analysis of steady state behaviour of the model and derived current derating laws calculated in off-line manner. The derating law is used as the terminal set in MPC which allows using one-step-ahead evaluation for efficient real-time implementation. The steady state analysis also provides coefficients for power loss balancing. The proposed approach is applied to control of dual converter, which has high redundancy of switching elements and, thus, wide space for optimization. It is shown in simulation that the proposed approach has better performance than previously published algorithms, at lower computational cost. Experimental evaluation of the algorithm performed on a converter prototype of rated power of 10 kW shows that the proposed controller is able to safely operate the converter near the thermal limit.

1 | INTRODUCTION

A dual inverter, also known as cascaded converter, or converter for open end winding load [1, 2] is widely used in application such as energy storage [3, 4] and renewable power sources [5]. The dual inverter [1] with an open-end winding induction machine is also an attractive concept in electric vehicle propulsion systems [6]. It produces twice higher voltage on the load with the same level of voltage stress on power semiconductors in comparison with a conventional two-level converter. Thus, it does not require a serial connection of battery cells and complex battery management design of the battery pack [7]. Another advantage is high redundancy in the number of switching combinations allowing improvement in current control. It allows current and torque ripple reduction [8], imbalanced load on dc-link sources [3, 4, 9], and compensation of zero voltage sequence [10]. On the other hand, the control strategies are then more complex and improper techniques may decrease its power utilization.

Many partial results for maximization of the power density of converters [11] and preserving its lifetime [12] have been proposed. These objectives can be achieved using maximum torque per ampere (MTPA) motor control strategy [13], utilizing proper thermal management of converter semiconductor elements [14], reducing thermal cycles [15] and balancing temperature among the semiconductor elements [16]. Maximum junction temperature can be also indirectly reduced by limiting and balancing power losses among the semiconductors [17]. Power losses mainly consist of conduction and switching losses. Switching losses can be reduced by implementation of discontinuous modulation techniques [9, 18, 19], variable pulse width modulator (PWM) carrier frequency [20], multilevel hysteresis-band direct torque control strategy [8], or by model predictive control (MPC) with cost function penalizing switching [21], [22]. More complex solution penalizing switching losses directly in the cost function can be utilized to improve trade off between the power losses and current ripple [23–25]. Another approach is to combine finite control set MPC (FCS-MPC) with space

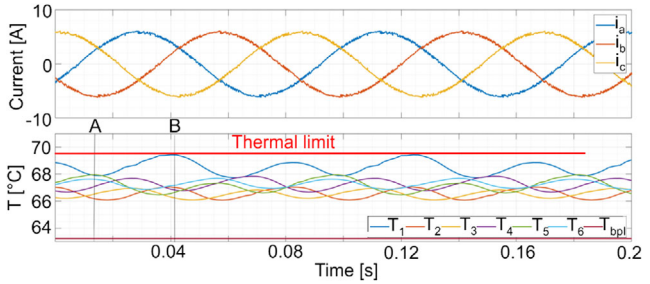

FIGURE 1 Example of temperature profile of converter elements during steady state operation of the drive at 5 Hz. T_{1-6} temperatures of s in the power module, T_{bpl} temperature of baseplate of the power module

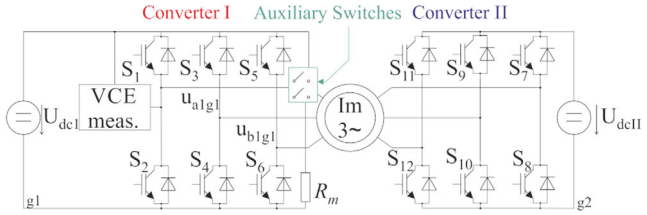

FIGURE 2 Power circuit of dual converter fed IM drive with indirect measurement of temperature of switch (IGBT) S_1 using VCE measurement at predefined current value (that is achieved using auxiliary switches replacing load with R_m, see Section 4.2)

vector PWM (SVPWM). SVPWM is used to pre-select suitable switching combinations and FCS-MPC is used to determine the optimal combination. This approach has been used for different types of converters [26–28].

A more complex problem is optimization of semiconductor thermal cycles, which exist on longer time scale. Improvement of thermal cycles can be achieved by varying power losses according to the junction temperature by changing switching frequency [29], gate-emitter voltage on IGBT [30] or output power [31]. A complex converter driver is needed in this case and it represents an significant disadvantage of this solution. An alternative solution is based on redistributing power losses of the semiconductor from elements with higher temperature to those with lower temperature. The idea behind the algorithm presented in [32] is that the semiconductors of the converter legs with higher current has higher temperature. Therefore, the cost of switching depends on the measured values of the current. More sophisticated approach is to model semiconductor temperature online based on a thermal model [33]. The modelled temperature can be used for multiple objectives such as increasing semiconductor module lifetime or balancing semiconductors temperature inside the module. The algorithm [33] redistributes power losses based on thermal model using MPC with short horizon and customized cost function. However, operation of an ac machine at the thermal limit of the converter is problematic since the temperatures of the converter elements fluctuate with frequency of the machine (see Figure 1 for illustration).

Looking at temperatures at point "A" in Figure 1, it may seem that the temperate is well under the thermal limit and it is possible to increase the input power of modules. However, doing so would yield violation of the thermal limit at point "B" in Figure 1, which can be only prevented by distortion of the current waveform. Since the number of steps between points "A" and "B" is 667, simple techniques of long-term MPC [34], such as heuristic preselection [28], or sphere decoding [35], would be prohibitively expensive to compute.

Therefore, analysis of the behaviour of the thermal model in the steady state of the drive and design a set of admissible operating points that do not yield violation of the thermal limit is proposed. This approach is closely related to classical derating techniques based on measured temperature in the converter [14], [36], where power losses are reduced by lowering current amplitude. While MPC has been used to design derating strategies, [37], it was done using high-level approach without considering the voltage model of the converter and the current model of the load. The closest related approach was presented in [38] where steady state temperature of the elements was estimated using low pass filters. However, the control strategy proposed in [38] used simple thermal model without considering cross-coupling between elements on the power module.

The main contribution is thus detailed analysis of the thermal model in steady state operation of the drive with focus on maximum temperatures of power electronics devices. The key result is translation of the thermal constraints in the MPC formulation into terminal set [39] and modification of the power balancing term using steady-state analysis. This allows to solve long-term optimization in one-step manner, which is in this application essential, since the number of unique switching combinations is 64. Specifically, semiconductor elements temperature balancing is achieved without evaluating the temperature model in the MPC. According to state of the art, this is the first use of this approach in thermally constrained predictive control.

The paper is organized as follows: All components of the system model are described in Section 2. Model predictive control is defined and analyzed in Section 3, where steady state analysis is used to derive simplified cost. The key element of the method is the thermal model which needs to be identified as described in Section 4.2. Simulation and experimental results are presented in Section 5.

2 | MODEL OF INDUCTION MACHINE DRIVE FED BY DUAL CONVERTER

Topology of the considered dual inverter [1] with a IGBT temperature monitoring and open-end winding induction machine (IM) as a load is displayed in Figure 2. The model of the whole system is now built from models of individual physical quantities: (i) electro-mechanical model, (ii) power losses, and (iii) thermal diffusion.

2.1 | Model of the motor and inverter

Mathematical models of all parts of the system that are important for full description of the proposed algorithm and are

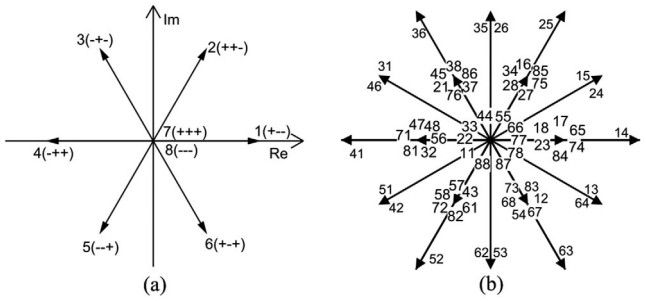

FIGURE 3 Converter output voltage vectors of single inverter (a) and dual inverter (b)

briefly described. The load current and the motor flux are modelled in the stationary reference frame of the motor [40]:

$$i_{s\alpha,k+1} = c i_{s\alpha,k} + d\Psi_{r\alpha,k} + e\omega_m \Psi_{r\beta,k} + f u_{\alpha,k}, \quad (1)$$

$$i_{s\beta,k+1} = c i_{s\beta,k} + d\Psi_{r\beta,k} - e\omega_m \Psi_{r\beta,k} + f u_{\beta,k}, \quad (2)$$

$$\Psi_{r\alpha,k+1} = \frac{R_r}{L_r} i_{s\alpha,k} + \left(1 - \frac{R_r}{L_r}\right)\Psi_{r\alpha,k} + p_p \omega_m \Psi_{r\beta,k}, \quad (3)$$

$$\Psi_{r\beta,k+1} = \frac{R_r}{L_r} i_{s\beta,k} + \left(1 - \frac{R_r}{L_r}\right)\Psi_{r\beta,k} + p_p \omega_m \Psi_{r\alpha,k}, \quad (4)$$

where $i_{s\alpha}, i_{s\beta}$ are components of the stator current vector, $\Psi_{r\alpha}, \Psi_{r\beta}$ are components of the rotor flux vector, ω_m is mechanical rotor speed, and p_p is number of pole-pairs. Parameters of the model are $c = 1 - (R_s + \frac{R_r L_h^2}{L_r^2})f$, $d = \frac{R_r L_h}{L_r^2} f$, $e = \frac{L_h p_p}{L_{rg}} f$, $f = \frac{\Delta t}{g}$, $g = L_{s\sigma} + L_{r\sigma}\frac{L_h}{L_r}$. Here, R_s is the stator resistance, R_r is the rotor resistance, L_h is the magnetizing inductance, L_r is the rotor inductance, L_s is the stator inductance, $L_{s\sigma}$ is the stator leakage inductance, $L_{r\sigma}$ is the rotor leakage inductance, Δt is the control sampling period, and $u_{\alpha,k}$ and $u_{\beta,k}$ are components of the stator voltage vector given by the converter phase voltages

$$u_\alpha = \frac{1}{3}\left(2\left(u_{a1g1} - u_{a2g2}\right) - u_{b1g1} + u_{b2g2} - u_{c1g1} + u_{c2g2}\right), \quad (5)$$

$$u_\beta = \frac{1}{\sqrt{3}}\left(u_{b1g1} - u_{b2g2} - u_{c1g1} + u_{c2g2}\right). \quad (6)$$

Note that the number of switching combinations providing the same value of the voltage vector is high, for example, zero voltage vector can be achieved by 10 switching combinations (see Figure 3(b)).

2.2 | Model of power losses

The model of power losses is based on a comprehensive guide [41] and simplified for the proposed algorithm. Specifically, semiconductor power losses are determined by conduction losses and switching losses. Other types of semiconductor losses are neglected. Power losses are modelled for 12 elements, where one element is a union of a IGBT and the associated freewheeling diode. This simplification is based on the assumption that the temperature of both junctions are close to each other. Note that this simplification is also conservative, since the power losses on both junctions contribute to the temperature of the element. Specifically, power losses of the x-th element, $x = 1, \ldots, 12$, in step $k+1$ are computed as

$$P_{x,k+1} = \begin{cases} P_{S_x,k+1} & \text{if } i_{x,k+1} > 0 \\ P_{D_x,k+1} & \text{otherwise} \end{cases} \quad (7)$$

$$\begin{aligned} P_{S_x,k+1} &= u_{T0T} i_{x,k+1} + r_{TT} i_{x,k+1}^2 \\ &\quad + \left(\chi_{on,k} K_{on} + \chi_{off,k} K_{off}\right) i_{x,k}, \\ P_{D_x,k+1} &= u_{T0D} i_{x,k+1} + r_{TD} i_{x,k+1}^2 + \chi_{rr,k} K_{rr} i_{x,k}, \end{aligned} \quad (8)$$

where P_{Sx} is the IGBT power loss of x-th element, P_{Dx} is the diode power losses of x-th element, i_x is x-th element current, u_{T0T} is the IGBT threshold voltage, u_{T0D} is the diode threshold voltage, r_{TT} is the open IGBT resistance, r_{TD} is the open diode resistance, $\chi_{on,k}$ indicates if the IGBT is switched on in time step k, $\chi_{off,k}$ indicates if the IGBT is turned off in time step k, $\chi_{rr,k}$ indicates if the diode is turned off in time step k, K_{on} is coefficient of IGBT turn on losses, K_{off} is coefficient of IGBT turn off losses, and K_{rr} is coefficient of diode reverse recovery losses.

2.3 | Model of thermal diffusion

The thermal model of [41] has been extended to consider coupling among individual IGBTs and diodes. It is assumed that semiconductors of converter I and converter II are located in two separated modules with separated heatsinks. The following notation will be used: $T_{y,k}$ is the junction temperature of y-th IGBT, $y = 1, \ldots, 12$, $T_{bpI,k}$ is the measured converter I baseplate temperature, $T_{bpII,k}$ is the converter II baseplate temperature, and $\Delta T_{y,k}$ is the modelled temperature difference between the y-th IGBT junction temperature and the corresponding baseplate temperature, that is,

$$\Delta T_{y,k} = T_{y,k} - T_{bpI,k} \qquad y = 1, \ldots, 6, \quad (9)$$

$$\Delta T_{y,k} = T_{y,k} - T_{bpII,k} \qquad y = 7, \ldots, 12. \quad (10)$$

The dynamics of the temperature difference for the IGBTs of converter I is considered to be a linear transfer function. Temperature of each element y is assumed to depend on n delayed values, and on contribution of power inputs of all its neighbours $x \in X_y = \{1, \ldots, 6\}$ for $y = 1, \ldots, 6$, and over $x \in X_y = \{7, \ldots, 12\}$ for $y = 7, \ldots, 12$. The influence of the power input is a weighted sum of m delayed value of the power input. This can be formally written as an autoregressive and regressive model of

orders n and m, respectively:

$$\Delta T_{y,k} = \sum_{v=1}^{n} -a_{y,n-v}\Delta T_{y,k-v} + \sum_{x\in X_y}\sum_{w=1}^{m} b_{yx,m-w}P_{x,k-w}. \quad (11)$$

Coefficients $a_{y,n-v}$ and $b_{yx,m-w}$ are model coefficients that will be identified from the data in section 4.2, $P_{x,k-w}$ are power losses of x-th element in the step $k-w$, where x is an index of an element of the converter.

3 | MODEL PREDICTIVE CONTROL OF DUAL INVERTER

The objective of the proposed control is to track the demanded load current in the d,q rotational reference frame linked to the rotor magnetic flux vector with the restriction of keeping all semiconductor junction temperatures below the maximum temperature T_{max}. The problem can be formulated as an optimization problem with the following cost:

$$g_t = g_{track} + g_{Tmax} + g_{imax}, \quad (12)$$

$$g_{track} = \left(i_{sd,t} - i^*_{sd}\right)^2 + \left(i_{sq,t} - i^*_{sq}\right)^2, \quad (13)$$

$$g_{imax} = 10^8\chi\left(i^2_{sd} + i^2_{sq} > I^2_{max}\right) \quad (14)$$

$$g_{Tmax} = 10^8\sum_{i=1}^{12}\chi\left(T_{x,t} > T_{max}\right), \quad (15)$$

where g_{track} is the term penalizing difference of the current vector components in rotating frame linked to the rotor magnetic flux from the requested values i^*_{sd} and i^*_{sq}, g_{imax} is safety limit penalizing violation of the maximum allowed current amplitude that has to be preserved at any time, its value $I_{max} = \sqrt{2}I_{CM,RMS}$ is given by the manufacturer [42], g_{Tmax} is hard limit penalizing violation of the maximum allowed temperature T_{max}, $\chi(\cdot)$ is an indicator function returning one if the argument is true, and zero otherwise. The motor current is controlled using the maximum torque per ampere strategy, hence, i^*_{sd} is equal to i^*_{sq}.

Since thermal model has a long time constant, the optimization should be performed on cost summed over a long horizon, that is, $g = \sum_{t=k+1}^{k+N} g_t$, for a large number of prediction steps N (see illustration in Figure 1). Computational complexity of direct optimization grows exponentially, which make this approach infeasible for the expected number of steps. Thus, the long horizon cost is often complemented by additional terms that helps to achieve good behaviour. For example, an additional term penalizing variance of temperatures was proposed in [33]. However, quality of the current tracking in the thermally constrained operation was not considered in [33]. Moreover, evaluation of the temperature model for all switching combinations is expensive. Therefore, additional terms of the cost function from steady state analysis at the thermal limit are proposed. In theory, it corresponds to design of a terminal set of model predictive control [39].

3.1 | Steady state analysis of thermal model

In this section, it is assumed that modules for both converters are identical and can analyze only model of converter I. In steady state, the difference between y-th IGBT temperature of converter I and its base plate is given by steady state of the thermal model (11) which can be computed analytically:

$$\Delta T_y = \sum_{x=1}^{6}\gamma_{yx}P_x, \qquad \gamma_{yx} = \frac{\bar{b}_{yx}}{\bar{a}_y} \quad (16)$$

$$\bar{a}_y = 1 + \sum_{v=1}^{n} a_{y,n-v}, \qquad \bar{b}_{yx} = \sum_{w=0}^{m} b_{yx,m-w}. \quad (17)$$

Here, P_x denotes steady state power losses of the xth element. Temperatures on the converter II are analogical. Equation (16) can be rewritten in matrix notation $\Delta\boldsymbol{T} = \Gamma\boldsymbol{P}$ where $\Delta\boldsymbol{T} = [\Delta T_1, \dots, \Delta T_6]$,$\boldsymbol{P} = [P_1, \dots, P_6]$ and 6x6 matrix Γ is composed of elements γ_{yx}.

Using matrix notation, the power losses that correspond to a given temperature profile can be computed

$$\boldsymbol{P} = \Gamma^{-1}\Delta\boldsymbol{T}. \quad (18)$$

For equal temperatures of all elements $\Delta\boldsymbol{T} = [T_{const}, \dots, T_{const}]$, the steady state power loss can be written as $P^*_x = \alpha_x T_{const}$ where α_x are constants given by the thermal model $[\alpha_1, \dots, \alpha_6]^T = \Gamma^{-1}\mathbf{1}$, and $\mathbf{1}$ denotes a vector of ones. This relation determines a ratio of power losses for a perfectly balanced thermal load.

Relation (18) can be computed offline and allows to design temperature balancing using power losses, and thus avoid expensive evaluation of the thermal model online.

First, it is assumed that the current tracking is almost perfect, that is, the actual current is close to the requested current i^*_s. Since power losses are dominated by the conduction losses, the sum of all losses $P_{sum} = \sum_x P_x$ is almost constant for all switching combinations. However, due to great flexibility of the dual converter, distribution of the power losses across the elements can be chosen.

Solution of (18) is an extreme of optimization problem

$$P^*_x = \min_{P_x}\sum_{x=1}^{6} P^2_x/\alpha_x, \quad \text{s.t.:} \sum_{x=1}^{6} P_x = P_{sum}, \quad (19)$$

under assignment $P_{sum} = T_{const}\sum_x \alpha_x$, which can be easily verified by optimality conditions of the corresponding Lagrangian. As mentioned above, the sum of all power losses is determined by the current. Therefore, balancing of temperatures can be achieved by optimization of cost

$$g_{bal} \approx g_{track} + \lambda_{bal}g_P, \qquad g_P = \min_{P_x}\sum_{x=1}^{6} P^2_x/\alpha_x, \quad (20)$$

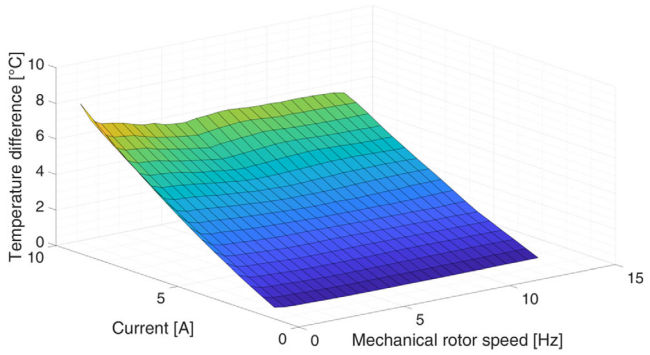

FIGURE 4 Simulated dependency of ΔT on motor speed and the stator current amplitude on a grid of admissible values. It will be used as a lookup table to obtain maximum current for given temperature difference and mechanical rotor speed

for very small values of λ_{bal} which has no effect of the current tracking but sufficient effect on power balancing.

Note, however, that such a perfect balancing is possible only when all elements conduct equally often, for example, for high speed operation of the drive. In low speeds, the power distribution is in conflict with current tracking. For example, only one current vector is requested at zero speed which greatly limits the elements that can be used, yielding imbalanced temperatures. Thus, this analysis cannot be used to guarantee maximum temperature and special treatment of overheating is necessary.

3.2 | Overheating protection

Prediction of the maximum temperature of the element on very long horizon is computationally demanding; therefore, it is proposed to evaluate the prediction offline for a wide range of operational conditions and store results in a lookup table (Figure 4). The prediction will take into account all effects of the problem, including load current, operating motor speed, switching frequency, and balancing using the proposed strategy. Specifically, a grid of stator current amplitude and mechanical rotor speed is created. Steady-state behaviour of the drive and maximum temperature difference, ΔT_y, that was achieved by any element during the simulation is evaluated for each grid-point and stored in the look-up table. As expected, the temperature difference grows with amplitude, but the rate of increase depends on the motor speed.

The lookup-table will be used in an inverse manner to find the maximum amplitude of the requested stator current (providing essentially derating of the drive) for a given rotor speed and maximum temperature

$$I^{**}_{max} = f(\omega_m, \Delta T_t). \tag{21}$$

Specifically, the $\Delta T_t = T_{max} - T_{bp,t}$ is computed in each step, and the current amplitude I^{**}_{max}, at which ΔT_t is reached in the lookup table, is computed for the current motor speed. If the temperature difference is larger than that in the table, the maximum current amplitude is set to $I^{**}_{max} = I_{max}$.

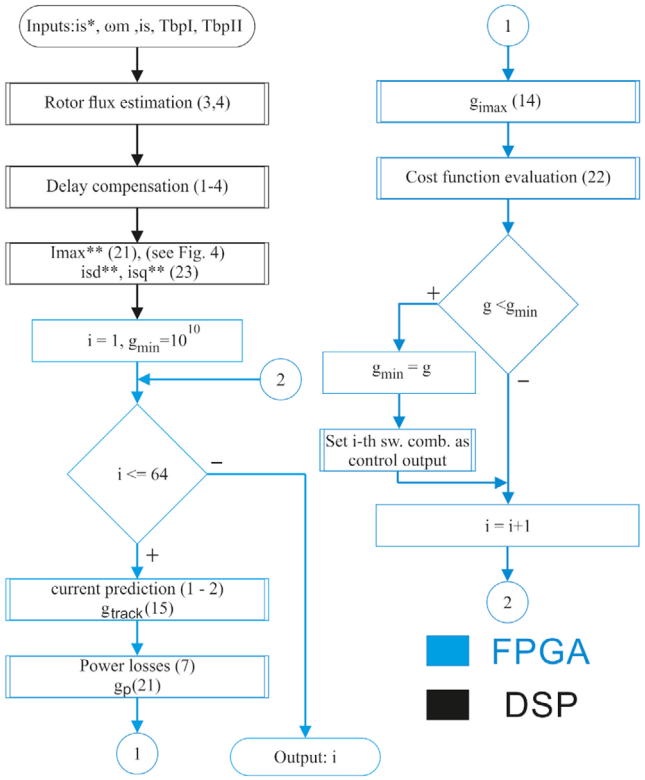

FIGURE 5 Flowchart of the proposed model predictive control

3.3 | Proposed cost function

Using the results of previous section, the final cost function is proposed as follows:

$$g_t = g_{track} + \lambda_{bal} g_P + g_{imax}, \tag{22}$$

where the g_{imax} and g_{Imax} are identical to those of (12), g_{track} is a modification of (13) using reference i^{**} with components

$$i^{**}_{sd} = i^{*}_{sd} \frac{I^{**}_{max}}{I_{max}}, \qquad i^{**}_{sq} = i^{*}_{sq} \frac{I^{**}_{max}}{I_{max}}, \tag{23}$$

instead of i^* because the current limit is now set by the overheat protection algorithm and changes during the converter operation, and g_P is given by (20). Note that the only tuning coefficient is λ_{bal} which should be set to a small value, as discussed in Section 3.1 and shown experimentally later. The control algorithm is summarized in Figure 5 in the form of a flowchart. Common operations such as measurement, rotor flux estimation (3, 4), delay compensation (1–4), and lookup table evaluation for I^{**}_{max} are performed on DSP. The FCS-MPC is evaluated on FPGA due to high number of switching combinations. For each switching combination, it is necessary to calculate the current prediction, power loss estimation, and all component of the cost function. At the end of the algorithm, the switching combination with the lowest value of cost function is selected as the control output.

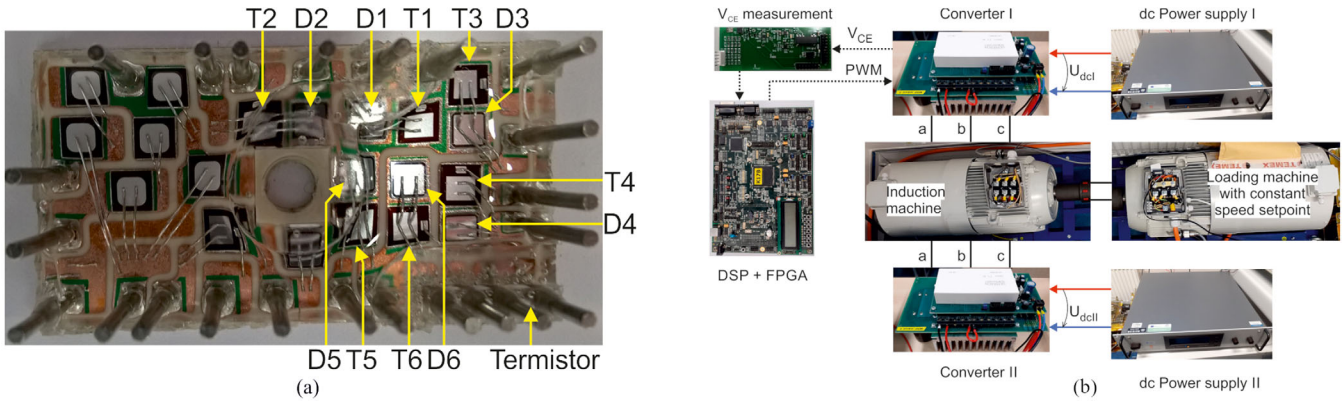

FIGURE 6 (a) Open module used in experiments with marked position of the modelled semiconductor elements; (b) simplified experimental setup

TABLE 1 Parameters of the experimental setup

Parameter name	Value
$L_{s\sigma}$ - Stator leakage inductance	3.57 mH
$L_{r\sigma}$ - Rotor leakage inductance	2.72 mH
L_h - Magnetizing inductance	93 mH
R_s - Stator resistance	0.408 Ω
R_r - Rotor resistance	1.12 Ω
Rated stator line-to-line voltage	400 V
Rated stator current	21 A
Rated motor mechanical speed	1470 rpm
Rated motor power	11 kW
Rated motor torque	71.46 Nm
p_p - Number of pole-pairs	2
$U_{dcI} = U_{dcII}$ - Converter dc-link voltage	60 V
Power electronics module	Semikron SK 20 DGDL 065 ET
V_{CES} - Maximum allowed V_{CE}	600 V
$I_{CM,RMS}$ - Maximum allowed current	24 A

4 | EXPERIMENTAL SETUP AND THERMAL MODEL IDENTIFICATION

Experiments were performed on two three-phase modules Semikron SK 20 DGDL 065 which is displayed in Figure 6(a). Parameters of the laboratory prototype are given in Table 1.

Two different experimental setups were used; the first one was used for the identification of the converter thermal model and the second one for the validation of identified data and for experimental verification of the proposed control. The scheme of the first setup is shown in Figure 7. For this experiment, only R-type 3-phase load is used to simply ensure defined current in the circuit. The experimental setup contains only one measuring device of V_{CE} and therefore, temperature of only one IGBT can be measured in one experiment. Assuming the identification of IGBT S_1 model parameters, both converters are connected to common dc-link supply U_{dcI}. Phases b and c are connected to the load resistors R, and phase a is connected to

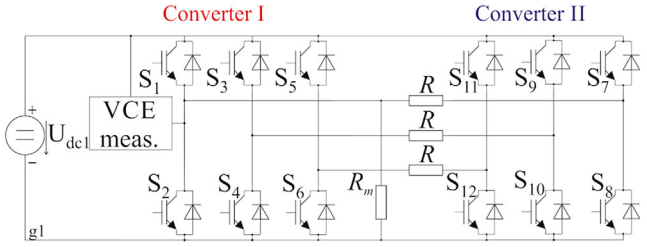

FIGURE 7 Modification of the power circuit for identification of thermal model of IGBT S_1 using R_m and V_{CE} measurement (see Section 4.2)

load R and to resistor for temperature measurement R_m. T_1 is monitored by measuring temperature-sensitive collector-emitter voltage V_{CE} [43]. Besides temperature, V_{CE} is highly dependent on the IGBT current, and therefore, the constant current during the V_{CE} measurement is ensured by connecting resistor R_m and disconnecting of the rest of the circuit except S_1. A similar approach can be used to obtain data for other IGBTs.

The second setup scheme, which is used for validation of the identified model using a different circuit configuration with an IM machine as the load, is shown in Figure 2. Each converter is powered by an independent power supply. For the temperature monitoring, the same method as in the identification experiments is used. The IM has high inductance which may influence the IGBT current and V_{CE} during temperature monitoring. Therefore, auxiliary switches are used to disconnect the motor phase from the converter. Overvoltage caused by breaking the circuit is suppressed by connecting the load to the positive pole of U_{dcI} before it is disconnected from the converter. Junction temperature is evaluated periodically every 3 s. Switching combination 77 (see Figure 3) is applied at the output of converter I and converter II during this junction temperature measurement. In steady state, the current flowing through the investigated IGBT is given by the U_{dcI}, R_m and V_{CE}. U_{dcI} and R_m are assumed to be constant. Therefore, the temperature can be evaluated as a function dependent only on V_{CE}. The dc-link voltage in the experiments is 60 V which is lower than the rated voltage. The reason for this choice is the low maximum allowed voltage at the input of the V_{CE} measurement circuit similar to [43]. Operation under higher voltage is identical. However, it

is not possible to provide validation of the temperature control. Moreover, the worst studied operating conditions occur in standstill and low motor speeds due to imbalanced heat transmission through the power semiconductor module. In these regimes, the motor back EMF voltage is low and 60 V is fully sufficient to demonstrate the performance.

4.1 | Computational issues

The drive controller includes both DSP (TI TMS320F28335) and FPGA (Altera cyclone III EP3C40Q240C8). Majority of the algorithm is implemented in the DSP; evaluation of the 64 switching combination is performed in the FPGA. Distribution of the algorithm parts between FPGA and DSP is illustrated in Figure 5. The part implemented in the DSP is outlined in black color and the part implemented in the FPGA is outlined in blue. The sampling period is 50 μs, execution time of the DSP code takes 33.75 μs, and evaluation of the FPGA part takes 0.83 μs.

4.2 | Thermal model identification

Since both converters are built from the same power modules, it is assumed that their thermal models are identical, and we identify only thermal model of converter I. The thermal model (11) with $n = 3$ and $m = 2$ is used. The model can be rewritten for a set of l data records in matrix form

$$\boldsymbol{Y}_y = \boldsymbol{A}_y \theta_y, \tag{24}$$

with assignments

$$\boldsymbol{Y}_y = \left[\Delta T_{y,4}, \Delta T_{y,5}, \ldots, \Delta T_{y,l}\right]^T,$$

$$\boldsymbol{A}_y = \begin{bmatrix} \boldsymbol{\Delta T}_{y,3} & \boldsymbol{P}_{1,3} & \boldsymbol{P}_{2,3} & \cdots & \boldsymbol{P}_{6,3} \\ \boldsymbol{\Delta T}_{y,4} & \boldsymbol{P}_{1,4} & \boldsymbol{P}_{2,4} & \cdots & \boldsymbol{P}_{6,4} \\ \vdots & \vdots & \vdots & & \vdots \\ \boldsymbol{\Delta T}_{y,l-1} & \boldsymbol{P}_{1,l-1} & \boldsymbol{P}_{2,l-1} & \cdots & \boldsymbol{P}_{6,l-1} \end{bmatrix},$$

$$\theta_y = \left[-\boldsymbol{a}_y, \boldsymbol{b}_{y1}, \boldsymbol{b}_{y2}, \boldsymbol{b}_{y3}, \boldsymbol{b}_{y4}, \boldsymbol{b}_{y5}, \boldsymbol{b}_{y6}\right]^T,$$

$$\boldsymbol{\Delta T}_{y,k} = \left[\Delta T_{y,k}, \Delta T_{y,k-1}, \Delta T_{y,k-2}\right],$$

$$\boldsymbol{P}_{y,k} = \left[P_{y,k}, P_{y,k-1}, P_{y,k-2}\right],$$

$$\boldsymbol{a}_y = \left[a_{y,2}, a_{y,1}, a_{y,0}\right]^T, \quad \boldsymbol{b}_{yx} = \left[b_{yx,2}, b_{yx,1}, b_{yx,0}\right]^T.$$

The data for converter thermal model identification were generated by a sequence of experiments, for which power losses of each element were calculated and temperature of a single IGBT measured. The measurement was repeated for all elements in the power module. Data from the experiment with measurement of IGBT T_1 temperature is displayed in Figure 8. The first subplot displays the measured IGBT temperature waveform and the second subplot shows average power losses of each element. Indirect measurement of the IGBT temperature via the V_{CE} is performed once every 40 ms for the period of 6 ms long. At this moment, S_1 is turned on and the load is disconnected using switches of converter II. In the remaining times, the switches are either ON to obtain maximum current through the load, or OFF according to the profile displayed in Figure 8. The experiment is repeated for each switch (IGBT) with reconnected V_{CE} circuit. From each experiment, we identified parameters of the transfer function of the y-th element using the least squares solution of (24):

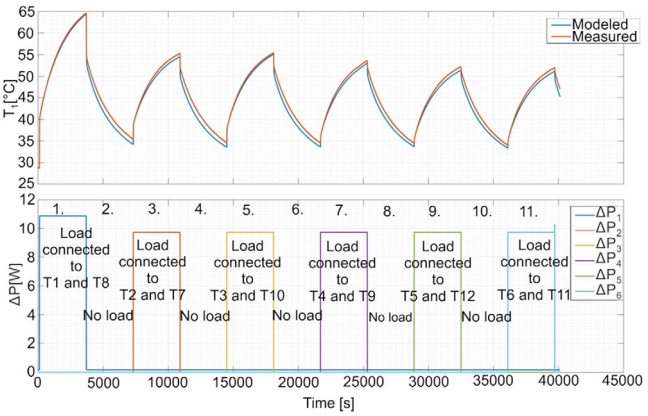

FIGURE 8 Measured waveform of T_1 and validation of the identified model. The top subplot compares the measured temperature (red) with predicted value (blue). The bottom subplot displays power losses during the experiment. Note that power losses of the first element are increased due to measurement of the V_{CE}

$$\hat{\theta}_{y,LS} = \left(\boldsymbol{A}_y^T \boldsymbol{A}_y\right)^{-1} \boldsymbol{A}_y^T \boldsymbol{Y}_y. \tag{25}$$

Validation of the model with identified parameters was done by forward simulation of the thermal profile from known initial conditions using only the measured base-plate temperature as input. The results for S_1 are displayed in Figure 8 in tandem with the measurements. Displayed waveforms can be divided into 12 parts according to the total power of the converter. In odd parts, one of IGBTs is turned on. In even parts, all IGBTs are turned off. Only one element temperature is measured during the experiment. The measurement is performed every 40 ms. Therefore, power losses of S_1 are higher due to V_{CE} measurement. Maximum difference between the measured and the simulated ΔT_1 is approximately 2°C.

5 | SIMULATIONS

In this section, simulation results of the proposed algorithm and comparison with the previously published one-step ahead approach [33], which has similar aims, that is, balancing of the temperatures and preserving maximum allowed temperature limit, are presented. However, it uses only one step-ahead MPC without the proposed precomputed steady-state results.

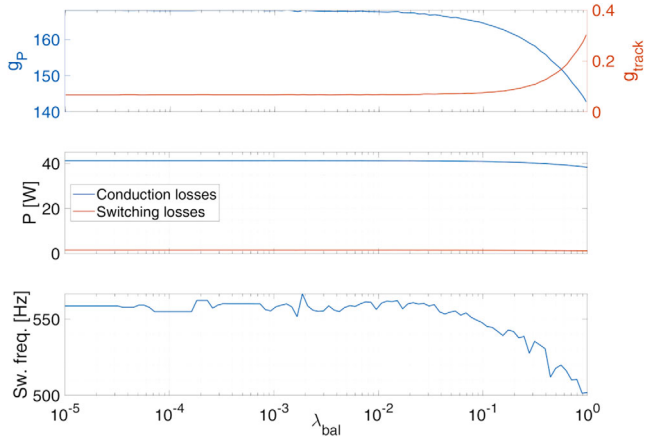

FIGURE 9 Sensitivity of the cost terms to penalization λ_{bal} for fixed sampling time Δt =50 μs. Top: terms of the cost function g_P and g_{track}. Middle: conduction and switching losses. Bottom: average switching frequency of one element

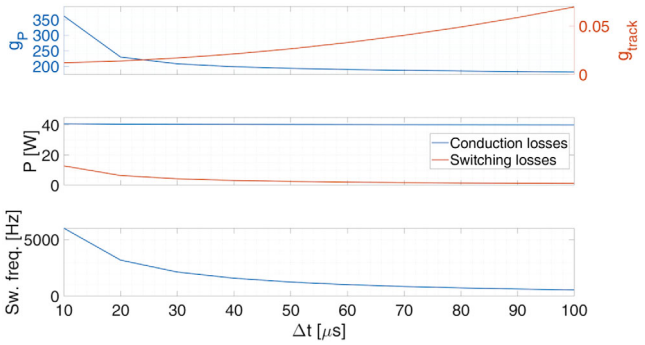

FIGURE 10 Sensitivity of the cost terms to sampling time Δt for fixed $\lambda_{bal} = 10^{-4}$. Top: terms of the cost function g_P and g_{track}. Middle: conduction and switching losses. Bottom: average switching frequency of one element

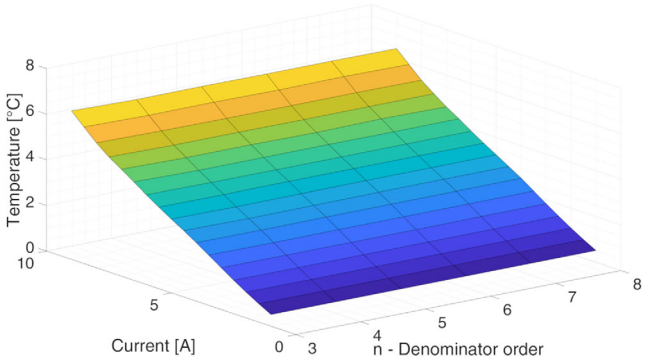

FIGURE 11 Simulated dependency of $\Delta T(n, I^*_{sm})$ with constant mechanical rotor speed of 5 Hz on a grid of admissible values.

Heat up of the converter was simulated with parameters given in Table 1, $m = 2, n = 3$ under steady operation with constant amplitude $i^*_{sd} = 5.66A$, $i^*_{sq} = 5.66A$, $T_{max} = 70°C$ and fixed mechanical rotor speed of $f_m = 5\,Hz$. The equality of the set-point $i^*_{sd} = i^*_{sq}$ is intentional to follow the Maximum Torque per Ampere criterion [13]. It is used in simulations as well as in experiments.

5.1 | Control parameters tuning

The only two adjustable parameters of the proposed method are λ_{bal} and Δt. In this section, validity of the assumptions of the theoretical analysis was tested by simulation. The tested scenario was simulated for different tuning of the penalization coefficient λ_{bal} and Δt. The sampling time Δt has direct influence on the switching frequency and it is thus used to study the effect of switching frequency on the result. However, similar sensitivity can be achieved by keeping the same sampling frequency and increasing penalization of the switching [21].

The tracking error, quality of temperature balancing and conduction and switching losses for all values of λ_{bal} are displayed in Figure 9. Note that the tracking error remains very low for values of $\lambda_{bal} < 10^{-2}$ and starts rising sharply when excessing 10^{-1}. Similarly, both switching and conduction losses are equal for penalizations below the critical value of λ_{bal}. This is in very good agreement with the theory and proves that the algorithm is insensitive to the choice of its penalization if $\lambda_{bal} < 10^{-2}$.

The effect of the switching frequency on the system performance is studied by varying the sampling time Δt in Figure 10. With increasing sampling time, the average switching frequency decreases, as well as the corresponding switching losses.

The sensitivity analysis of the system performance on Δt has shown that both switching losses and current tracking error are dependent on Δt. Note that for the investigated system, reducing Δt below 40 μs has only slight effect on tracking error but it significantly increased switching losses (and thus the g_P term of the cost). The conductive losses remain unaffected but the current tracking error is increased. From this analysis, we choose our operating point to be $\Delta t = 50\,\mu s$ and $\lambda_{bal} = 10^{-4}$ which offers a satisfying trade of between power losses and current tracking.

5.2 | Sensitivity study

In this section, a sensitivity study of the precomputed temperatures to parameters of the thermal model and the chosen sampling period is provided. The dependence of the predicted temperature on thermal model order is displayed in Figure 11. Note that the resulting temperature is rather insensitive to the model order. Therefore, the third order thermal model is used. The dependence of the predicted temperature on the sampling time (and thus switching frequency) is displayed in Figure 12. In this case, the temperature rises significantly for very low sampling times due to increased switching losses (see Figure 10). This indicates that if the switching frequency significantly varies, the precomputed lookup table should contain switching frequency as one of the dimensions.

The lookup table was derived using nominal identified values of the thermal model. While heat transfer models are relatively stable, it is still possible that the identification experiment was not ideal and the estimated thermal coefficients differ from the

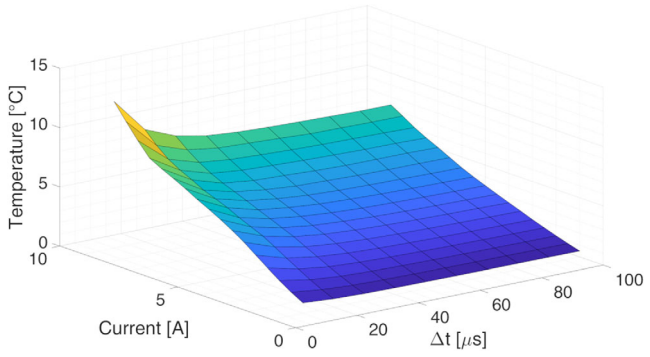

FIGURE 12 Simulated dependency of $\Delta T(\Delta t, I^*_{sm})$ with constant mechanical rotor speed of 5 Hz on a grid of admissible values

real ones. Experimental comparison of application of the algorithm based on the identified coefficients when applied to real system with different parameters was performed and results are presented in Figure 13. Specifically, the mismatch was in coefficients a_y from Equation (11). The lookup table uses their estimated value. Parameters of the controlled "true" system in simulation were changed to $a_{y,sim} = 0.8a_y$, and $a_{y,sim} = 1.2a_y$ for all time delays to simulate lower heat dissipation and higher heat dissipation than was identified. As expected, when the real dissipation was lower than identified (Figure 13(a)), the temperature limit was violated. On the other hand, when the real dissipation was higher than estimated, the derating was more aggressive and the temperature limit was not reached (Figure 13(b)).

5.3 | Comparison with state of the art approach

The proposed algorithm is compared to state-of-the-art algorithm for the same purpose proposed in [33] under two operational scenarios. First, heat-up of the converter loaded with periodic duty cycles of 8 A for 150 s and 0 A for 100 s are simulated and the results displayed for the previously published MPC [33] in Figure 14(a) and for the proposed MPC in Figure 14(b). Note that both algorithms preserve the temperature of the semiconductors below the limit and both algorithm are able to balance among the IGBTs without affecting the current tracking ability.

Challenges arise during the second scenario, converter heat-up after the start-up with the converter load of 8 A when the temperature limit is reached. Simulation results are shown for previously published MPC [33] in Figure 15(a) and for the proposed MPC in Figure 15(b). Current waveforms for operation at the maximum allowed temperature are shown for both algorithms in Figure 16. For the previously published MPC, the hard limit on temperature disables switching combinations which would lead to semiconductor over-temperature. When the setpoint is reached too fast, no switching combination can decrease the temperature due to thermal inertia and the combination with the lowest increase is zero. The converter is thus off until the temperature falls below the thermal limit. A potential

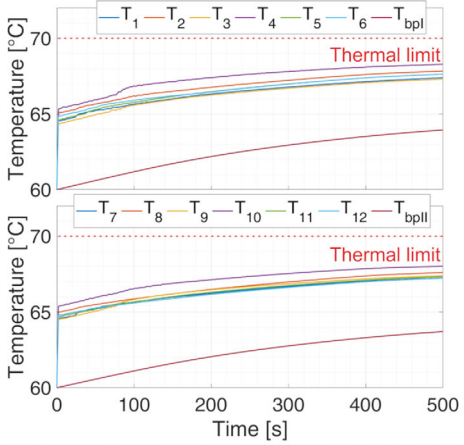

(a) Simulated "true" thermal model with low heat dissipation, $a_{y,sim} = 0.8a_y$

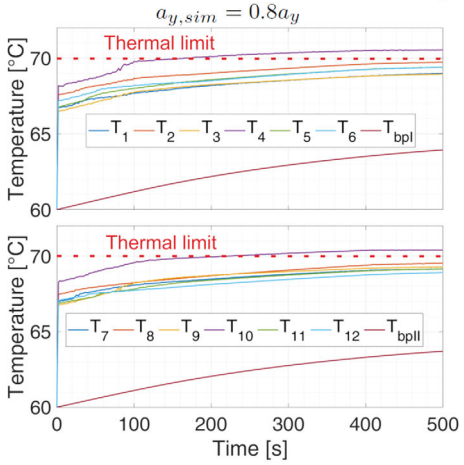

(b) Simulated "true" thermal model with high heat dissipation, $a_{y,sim} = 1.2a_y$

FIGURE 13 Simulated heatup of the converter under thermal model mismatch for two cases: lower heat dissipation than identified simulated by multiplying all a_y coefficients of the thermal model by 0.8 (a); higher heat dissipation than identified simulated by multiplying all a_y coefficients of the thermal model by 1.2 (b)

remedy of this degenerative behaviour would include additional heuristic penalization. On the other hand, the proposed control evaluates the power losses for the whole waveform (see Section 3.1) which limits on the current amplitude in advance. The critical semiconductor temperature is never reached, no switching combination disabled and the current waveform is not distorted.

Other differences are negligible, and the results are considered to be comparable in these operating conditions. Both approaches achieve homogeneous temperature profiles, but the proposed algorithm needs to evaluate only the power losses, while the previously published method needs to evaluate the temperature model which is much more computationally expensive. The computational cost was evaluated in MATLAB for both algorithms for 30,000 steps. The execution time of a single step is evaluated as the total execution time of the whole simulation divided by the number of steps. Execution time of the previous algorithm is 220 μs while that of the proposed algorithms is only 22 μs.

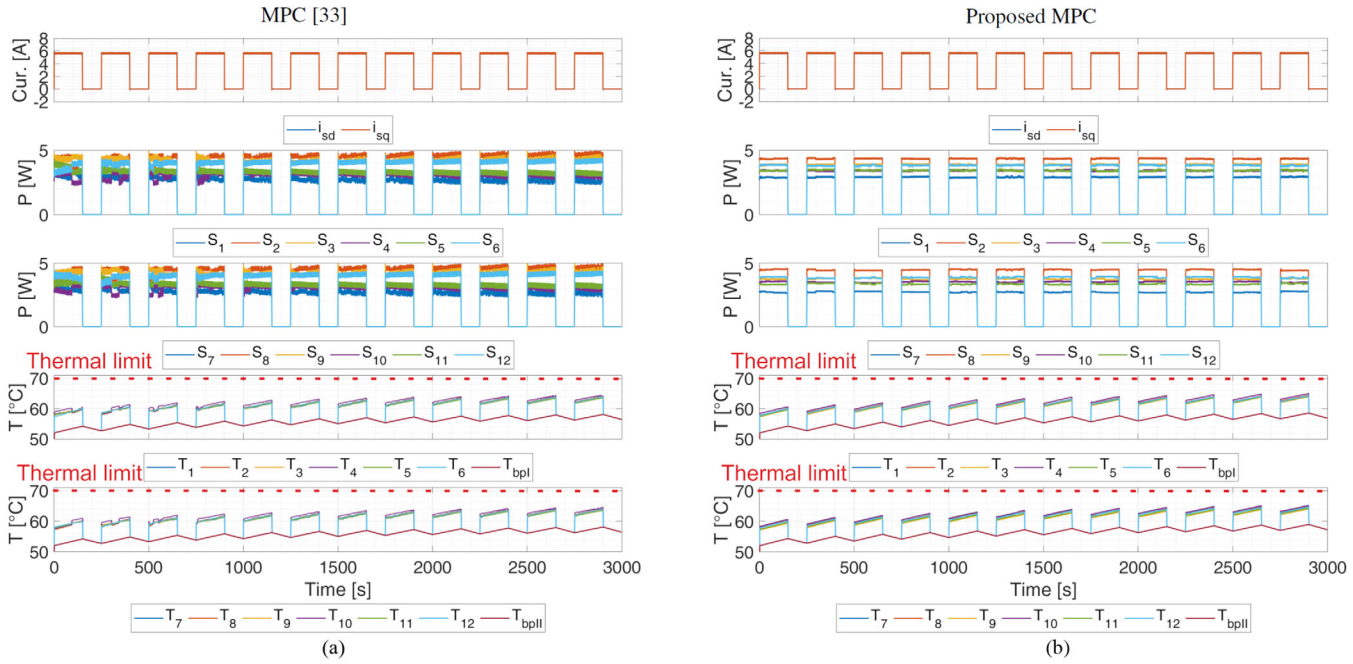

FIGURE 14 Simulated heat up of the dual converter under fixed mechanical rotor speed of 5 Hz with periodic duty load of 8 A for the previously published MPC [33] (a) and for the proposed algorithm (b). Top: The output current in d-q coordinate frame. Second row: Power losses of the elements of converter I. Third row: Power losses of the elements of converter II. Fourth row:. Temperatures T_{1-6} and T_{bpI} of converter I. Bottom: Temperatures T_{7-12} and T_{bpII} of converter II

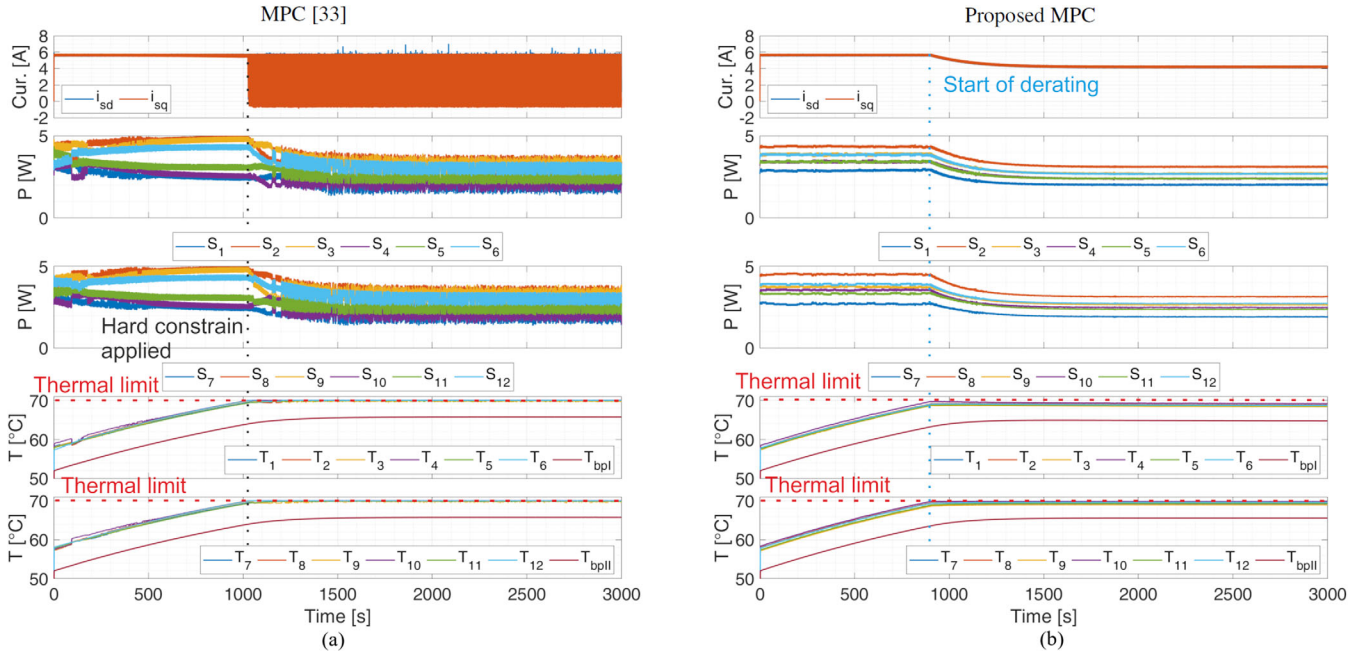

FIGURE 15 Simulated heat up of the dual converter under fixed mechanical rotor speed of 5 Hz with load current of 8 A when converter temperature limit is reached. Results for the previously published MPC [33] are shown in (a) and for the proposed algorithm in (b). Top: The output current in d-q coordinate frame. Second row: Power losses of the elements of converter I. Third row: Power losses of the elements of converter II. Fourth row:. Temperatures T_{1-6} and T_{bpI} of converter I. Bottom: Temperatures T_{7-12} and T_{bpII} of converter II

Similar simulation with results shown in Figure 17 was performed for the standstill operation, which is the worst case for temperature balancing. The results are analogous to those in Figure 15. The major disadvantage of MPC [33] is again current distortion caused by applying the thermal limits. Note, however, that detailed modelling of the temperature of [33] in this case, allows to reach the thermal limit very precisely. However, it is achieved at the cost of distorted current. The proposed

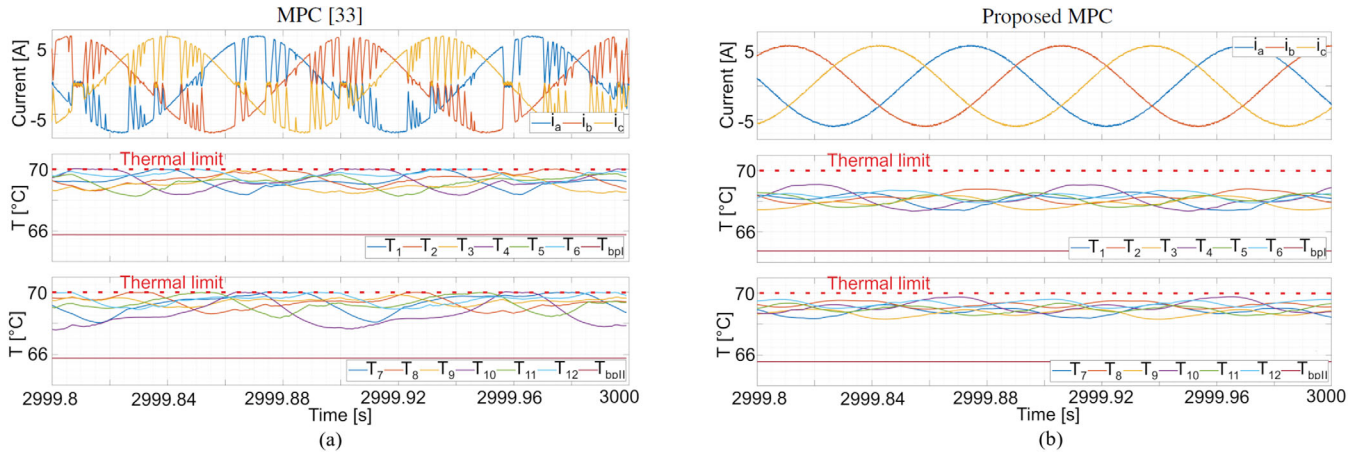

FIGURE 16 Detail of simulated stator phase currents in the steady state operation on thermal limit of the dual converter with rotating IM drive at mechanical rotor speed of 5 Hz for two control strategies: the previously published MPC [33] (a) and the proposed algorithm (b)

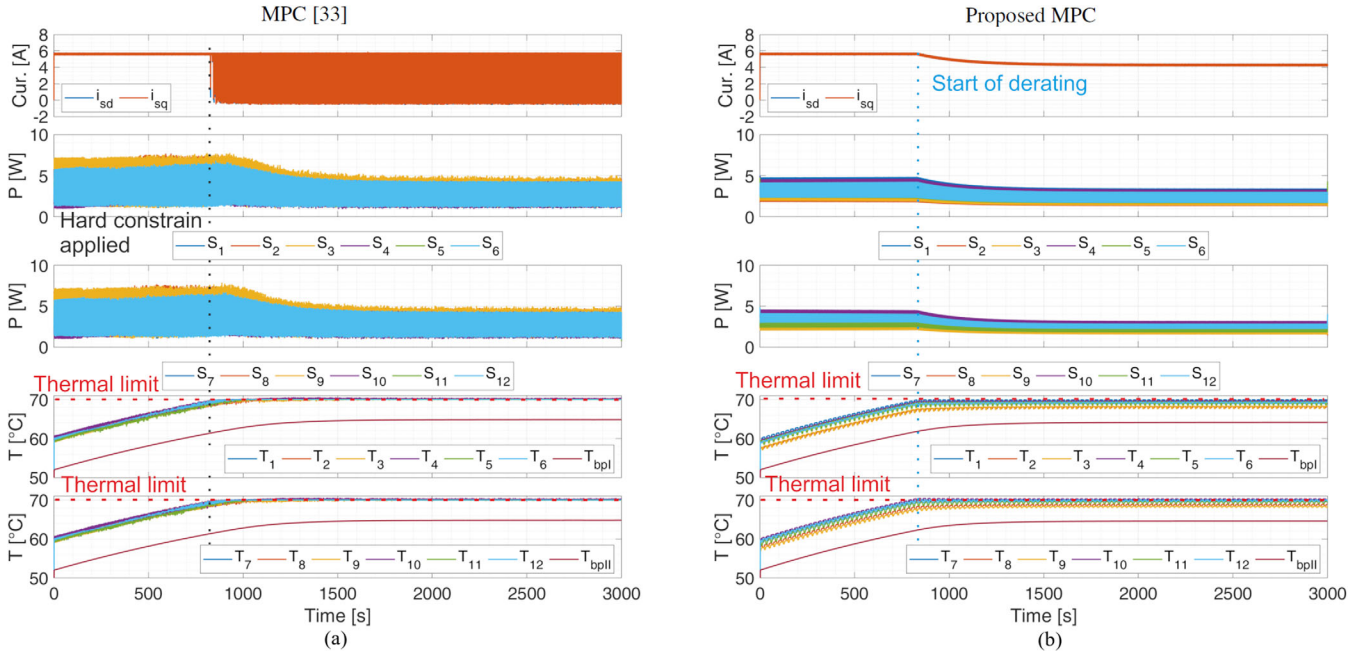

FIGURE 17 Simulated heat up of the dual converter under standstill operation with load current of 8 A when converter temperature limit is reached. Results for the previously published MPC [33] are shown in (a) and for the proposed algorithm in (b). Top: The output current in d-q coordinate frame. Second row: Power losses of the elements of converter I. Third row: Power losses of the elements of converter II. Fourth row: Temperatures T_{1-6} and T_{bpI} of converter I. Bottom: Temperatures T_{7-12} and T_{bpII} of converter II

control strategy thus prioritize the current waveform over reaching exactly the thermal limit.

6 | EXPERIMENTS

Experiments were done on the test rig described in Section 4.2. Since only one V_{CE} measurement is available, only temperature of T1 IGBT is measured. The measurement is not used in the control algorithm, it is used only to validate the correct function of the proposed algorithm.

6.1 | Operation at mechanical rotor speed of 5 Hz

The results for operation at mechanical rotor speed $f_m = 5\,Hz$ in torque control mode (with the motor shaft coupled to a loading IM drive with constant speed control setpoint) are shown for periodic duty with high load of $8\,A$ for $200\,s$ in Figure 18(a) and low load ($0\,A$ or $3\,A$) for $100\,s$ in Figure 18(b). During periodic duty load with low load of $0\,A$, the converter is able to cool down during no load intervals. Therefore, the temperature limit is not reached and current derating is

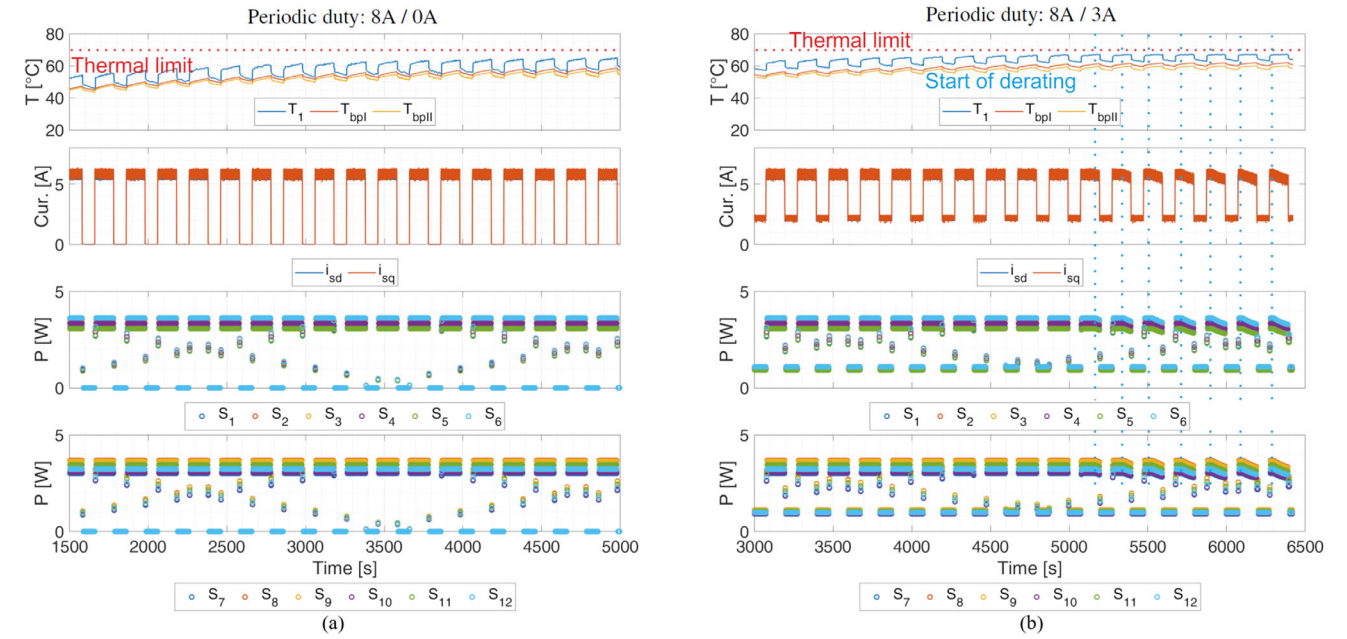

FIGURE 18 Experimental results for the proposed MPC in operation $f_m = 5\,Hz$ with periodic duty switching high load of 8A for 20 min with low load of $0\,A$ (a) or $3\,A$ (b) for 5 min. Top: measured T_1 junction temperature (blue curve), converter I baseplate temperature (red curve) and converter II baseplate temperature (orange curve). Upper middle: d-q components of the measured load current. Lower middle: power losses of each element of converter I. Bottom: power losses of each element of converter II

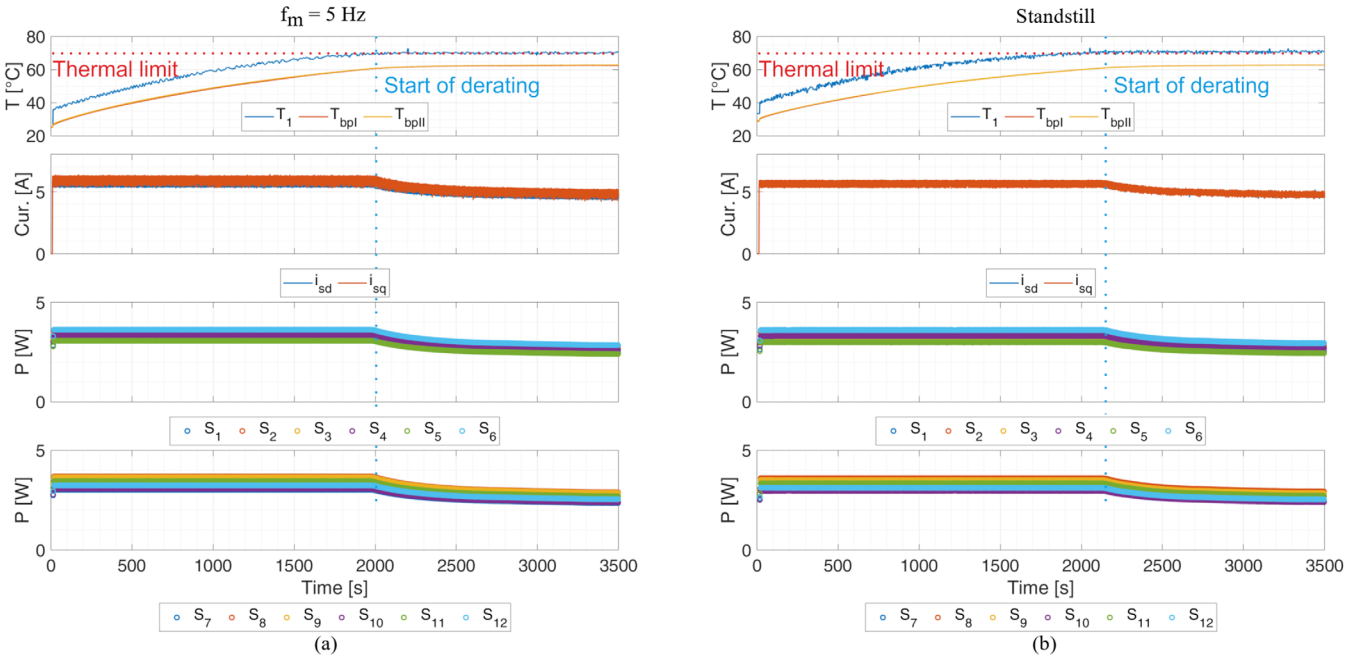

FIGURE 19 Experimental results for the proposed MPC in constant load operation of 8 A under $f_m = 5\,Hz$ (a) and standstill (b). Top: measured T_1 junction temperature (blue curve), converter I baseplate temperature (red curve) and converter II baseplate temperature (orange curve). Upper middle: d-q components of the measured load current. Lower middle: power losses of each element of converter I. Bottom: power losses of each element of converter II

inactive. The power losses are imbalanced according to the α_x. Increasing the low load current to $3\,A$ implies higher thermal stress and the derating becomes active at the end of the experiment.

Even more demanding regime occurs during the continuous load of $8\,A$ with mechanical rotor speed $f_m = 5\,Hz$, in Figure 19(a), and the continuous load of 8 A at standstill (0 Hz) in Figure 19(b). At first, the converter is loaded with maximum

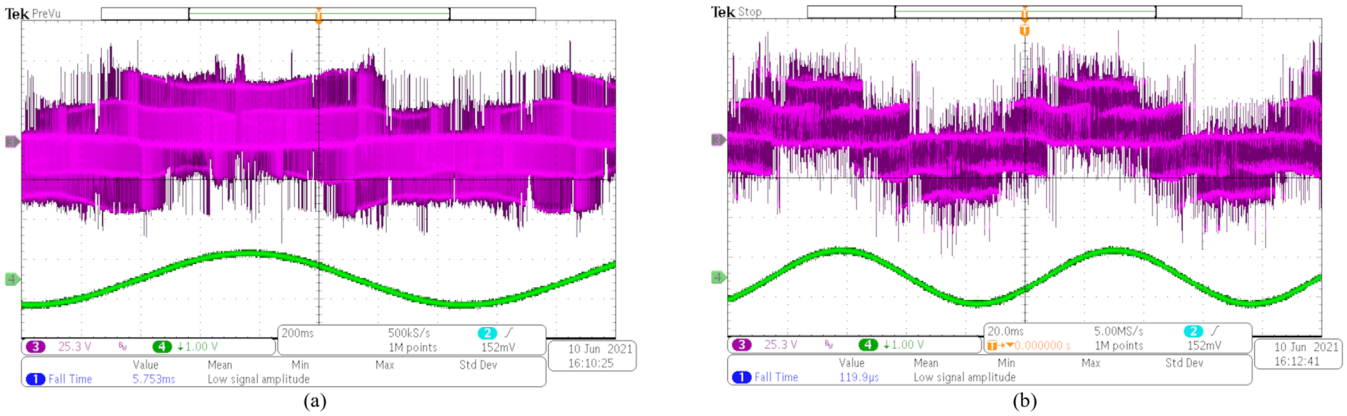

FIGURE 20 Experimental results for the proposed MPC in steady state under standstill operation (a) and $f_m = 5\,Hz$ (b). Magenta: phase load voltage; green: phase current

allowed current. The temperature of IGBTs rises, and the losses are constant according to the load current. When the temperature limit is reached (around $t = 2000\,s$), the current amplitude of the proposed control is reduced by the derating term. Its consequence is that the losses in the IGBTs and freewheeling diodes slightly decrease. After this, the temperature of the IGBTs stops at the temperature limit, which is set to 70°C. The converter then operates on this temperature limit. Comparing standstill operation with operation at $f_m = 5\,Hz$, standstill operation has both current amplitude and heatsink temperature lower. Note that this result was obtained without using the measured junction temperature as a feedback. Steady state phase load voltage waveform and steady state phase current waveform for both operations are shown in Figure 20. The results shows that the inverter is capable to maintain low current distortion when the overheat protection is applied.

6.2 | Experimental heat-up at standstill operation

The proposed control was tested at standstill operation (the motor locked by a mechanical brake) with the requested stator current of $8\,A$. The results are shown in Figure 19. At the beginning, the junction temperature is low, therefore, no limits are applied. With rising temperature, both power losses and current amplitude are limited. The junction temperature measured by V_{CE} is always below the chosen thermal limit of 70°C. It can be seen from experimental results (Figure 19) that the limit temperature is set to 70°C and the proposed control strategy stabilizes the IGBT temperature within an interval ±1°C around this limit.

7 | CONCLUSIONS

The paper presents a control algorithm based on FCS-MPC for maximum power utilization of dual inverter. The control is designed with two main objectives: (i) load current tracking; (ii) keeping the junction temperatures of converter power electronics devices below a prescribed limit. Due to long time constants of the thermal model, the prediction horizon would have to be very long. To achieve computationally affordable algorithm, the use of steady state analysis to approximate the cost on long horizon and derive a terminal set that is used as a cost term in one-step ahead MPC is proposed. Moreover, it is shown that the steady state analysis of the thermal model allows to design penalization coefficients for balancing the power losses between the converter elements, thus avoiding any manual tuning. The algorithm ability to maximize semiconductor utilization was verified by experiments using indirect measurement of the junction temperature. Compared to the previously published solution the proposed solution:

- is more accurate than the previously published solution using only one-step ahead cost function,
- is significantly faster to compute on-line,
- has only one tuning coefficient in the cost function which is thus easier to tune,
- requires to pre-compute and store a lookup table by simulation.

The presented approach of precomputing the steady state balancing coefficients and derating laws is very general and can be applied to many different topologies and transistor types (e.g. IGBT, MOSFET). It can be coupled with the proposed one-step ahead FCS-MPC, multi-step ahead FCS-MPC for higher accuracy, or with PWM-based control techniques for lower computational cost. In temperature critical applications, the indirect temperature measurement can be used for all elements and also included in the feedback.

FUNDING

This research has been supported by the Ministry of Education, Youth and Sports of the Czech Republic under the project OP VVV Electrical Engineering Technologies with High-Level of Embedded Intelligence CZ.02.1.01/0.0/0.0/18_069/0009855

ORCID

Martin Votava https://orcid.org/0000-0001-5762-7646
Vaclav Smidl https://orcid.org/0000-0003-3027-6174
Tomas Glasberger https://orcid.org/0000-0003-1406-6513

REFERENCES

1. Corzine, K., Sudhoff, S., Whitcomb, C.: Performance characteristics of a cascaded two-level converter. IEEE Trans. Energy Convers. 14(3), 433–439 (1999)
2. Baranwal, R., Basu, K., Mohan, N.: Carrier-based implementation of SVPWM for dual two-level VSI and dual matrix converter with zero common-mode voltage. IEEE Trans. Power Electron. 30(3), 1471–1487 (2015)
3. Jayasinghe, S.G., Vilathgamuwa, D.M., Madawala, U.K.: A dual inverter-based supercapacitor direct integration scheme for wind energy conversion systems. IEEE Trans. Ind. Appl. 49(3), 1023–1030 (2013)
4. Jayasinghe, S., Vilathgamuwa, D.: Dual inverter system with integrated energy storage for grid connected photovoltaic systems. In: 2015 IEEE 11th International Conference on Power Electronics and Drive Systems, pp. 796–803. IEEE, Piscataway, NJ (2015)
5. Oleschuk, V., et al.: Schemes and techniques of synchronous modulation of PV inverters with high modulation indices: A survey. In: 2021 12th International Symposium on Advanced Topics in Electrical Engineering (ATEE), pp. 1–6. IEEE, Piscataway, NJ (2021)
6. Shi, R., Semsar, S., Lehn, P.W.: Constant current fast charging of electric vehicles via a DC grid using a dual-inverter drive. IEEE Trans. Ind. Electron. 64(9), 6940–6949 (2017)
7. Narayanaswamy, S., et al.: Modular active charge balancing for scalable battery packs. IEEE Trans. Very Large Scale Integr. VLSI Syst. 25(3), 974–987 (2017)
8. Meesala, R.E.K., Thippiripati, V.K.: An improved direct torque control of three-level dual inverter fed open-ended winding induction motor drive based on modified look-up table. IEEE Trans. Ind. Electron. 35(4), 3906–3917 (2019)
9. Lakhimsetty, S., Surulivel, N., Somasekhar, V.: Improvised SVPWM strategies for an enhanced performance for a four-level open-end winding induction motor drive. IEEE Trans. Ind. Electron. 64(4), 2750–2759 (2016)
10. Li, A., et al.: A generalized carrier-based pwm with zero-axis voltage elimination for open-end winding motor drive. In: 2020 IEEE Energy Conversion Congress and Exposition (ECCE), pp. 5336–5340. IEEE, Piscataway, NJ (2020)
11. Drofenik, U., Laimer, G. & Kolar, J.W. : Theoretical converter power density limits for forced convection cooling. In: Proceedings of the International PCIM Europe 2005 Conference, pp. 608–619. ZM Communications, Nurnberg, Germany (2005)
12. Yang, S., et al.: An industry-based survey of reliability in power electronic converters. IEEE Trans. Ind. Appl. 47(3), 1441–1451 (2011)
13. Liu, Y., Bazzi, A.: Improved maximum torque-per-ampere control of induction machines by considering iron loss. In: 2017 IEEE international electric machines and drives conference (IEMDC), pp. 1–6. IEEE, Piscataway, NJ (2017)
14. Robinson, F.V.P.: Maximising device current utilisation in inverter drives. In: Power Electronics and Variable-Speed Drives, 1994. Fifth International Conference on, pp. 580–585. IEEE, Piscataway, NJ (1994)
15. van der Broeck, C.H., et al.: Methodology for active thermal cycle reduction of power electronic modules. IEEE Trans. Power Electron. 34, 8213–8229 (2018)
16. Hauk, E., et al.: New junction temperature balancing method for a three level active NPC converter. EPE J. 22(2), 6–12 (2012)
17. Zhang, B., et al.: A new pwm scheme for loss balancing and neutral-point voltage balancing in three-level active NPC converter. In: Industrial Electronics and Applications (ICIEA), 2015 IEEE 10th Conference on, pp. 1128–1133. IEEE, Piscataway, NJ (2015)
18. Ojo, O.: The generalized discontinuous PWM scheme for three-phase voltage source inverters. IEEE Trans. Ind. Electron. 51(6), 1280–1289 (2004)
19. Monopoli, V.G., et al.: Improved harmonic performance of cascaded h-bridge converters with thermal control. IEEE Trans. Ind. Electron. 66(7), 4982–4991 (2018)
20. Jiang, D., Wang, F.: Variable switching frequency PWM for three-phase converters based on current ripple prediction. IEEE Trans. Power Electron. 28(11), 4951–4961 (2013)
21. Rodriguez, J., Cortes, P.: Predictive Control of Power Converters and Electrical Drives, vol. 40. John Wiley & Sons, Hoboken, NJ (2012)
22. Liu, P., et al.: Model predictive control for quasi-z source inverters with improved thermal performance. In: 2018 IEEE 19th Workshop on Control and Modeling for Power Electronics (COMPEL), pp. 1–6. IEEE, Piscataway, NJ (2018)
23. Novak, M., Dragicevic, T., Blaabjerg, F.: Finite set MPC algorithm for achieving thermal redistribution in a neutral-point-clamped converter. In: IECON 2018-44th Annual Conference of the IEEE Industrial Electronics Society, pp. 5290–5296. IEEE, Piscataway, NJ (2018)
24. Novak, M., et al.: FS-MPC based thermal stress balancing and reliability analysis for NPC converters. IEEE Open J. Power Electron. 2, 124–137 (2021)
25. Wang, L., et al.: Finite control set model predictive control with secondary problem formulation for power loss and thermal stress reductions. IEEE Trans. Ind. Appl. 56(4), 4028–4039 (2020)
26. Aly, M., Dousoky, G.M., Shoyama, M.: Design and validation of svpwm algorithm for thermal protection of t-type three-level inverters. In: Telecommunications Energy Conference (INTELEC), 2015 IEEE International, pp. 1–6. IEEE, Piscataway, NJ (2015)
27. Aly, M., et al.: A unified SVM algorithm for lifetime prolongation of thermally-overheated power devices in multi-level inverters. In: Energy Conversion Congress and Exposition (ECCE), 2016 IEEE, pp. 1–6. IEEE, Piscataway, NJ (2016)
28. Votava, M., et al.: Improved SV PWM for dual inverter with real-time minimization of converter power losses. In: Power Electronics and Applications (EPE'17 ECCE Europe), 2017 19th European Conference on, pp. P–1. IEEE, Piscataway, NJ (2017)
29. Saleki, A., et al.: Lifetime extension by varying switching frequency of inverters based on junction temperature estimation. In: 2018 9th Annual Power Electronics, Drives Systems and Technologies Conference (PEDSTC), pp. 259–264. IEEE, Piscataway, NJ (2018)
30. Andresen, M., et al.: Junction temperature control for more reliable power electronics. IEEE Trans. Power Electron. 33(1), 765–776 (2018)
31. Andresen, M., et al.: Active thermal control of asynchronously-connected grids considering load sensitivity to voltage. In: 2018 IEEE Energy Conversion Congress and Exposition (ECCE), pp. 4070–4077. IEEE, Piscataway, NJ (2018)
32. Novak, M., Blaabjerg, F.: Model predictive active thermal control strategy for lifetime extension of a 3L-NPC converter for UPS applications. In: 2020 IEEE 21st Workshop on Control and Modeling for Power Electronics (COMPEL), pp. 1–7. IEEE, Piscataway, NJ (2020)
33. Falck, J., Buticchi, G., Liserre, M.: Thermal stress based model predictive control of electric drives. IEEE Trans. Ind. Appl. 54(2), 1513–1522 (2018)
34. Rodriguez, J., et al.: State of the art of finite control set model predictive control in power electronics. IEEE Trans. Ind. Inf. 9(2), 1003–1016 (2013)
35. Geyer, T., Quevedo, D.E.: Multistep finite control set model predictive control for power electronics. IEEE Trans. Power Electron. 29(12), 6836–6846 (2014)
36. Blasko, V., Lukaszewski, R., Sladky, R.: On line thermal model and thermal management strategy of a three phase voltage source inverter. In: Conference Record of the 1999 IEEE Industry Applications Conference. Thirty-Fourth IAS Annual Meeting, vol. 2, pp. 1423–1431. IEEE, Piscataway, NJ (1999)
37. Wallscheid, O., Böcker, J.: Derating of automotive drive systems using model predictive control. In: 2017 IEEE International Symposium on Predictive Control of Electrical Drives and Power Electronics (PRECEDE), pp. 31–36. IEEE, Piscataway, NJ (2017)
38. Lemmens, J., Vanassche, P., Driesen, J.: Optimal control of traction motor drives under electrothermal constraints. IEEE J. Emerging Sel. Top. Power Electron. 2(2), 249–263 (2014)

39. Mayne, D.Q., et al.: Constrained model predictive control: Stability and optimality. Automatica 36(6), 789–814 (2000)
40. Rehman, H., et al.: A new current model flux observer for wide speed range sensorless control of an induction machine. IEEE Trans. Power Electron. 17(6), 1041–1048 (2002)
41. Wintrich, A., et al.: Semikron: Application Manual Power Semiconductors. ISLE, Ilmenau (2011)
42. 3-phase bridge rectifier + brake chopper +3-phase bridge inverter sk 20 dgdl 065 et. (2008)
43. Nowak, M., Rabkowski, J., Barlik, R.: Measurement of temperature sensitive parameter characteristics of semiconductor silicon and silicon-carbide power devices. In: 2008 13th International Power Electronics and Motion Control Conference, pp. 84–87. IEEE, Piscataway, NJ (2008)

How to cite this article: Votava M, Smidl V, Peroutka Z, Glasberger T. Maximizing power utilization of dual converter using predictive control with steady state cost. IET Power Electron. 1–15 (2021).
https://doi.org/10.1049/pel2.12174